Efficient organic X-ray scintillators achieved by hybridized local and charge-transfer emitters with through-space heavy atom-π interactions

Chensen Li[1,2,6], Yaohui Li[3,6], Minghui Wu[4,6], Fancheng Kong[5], Binxia Jia[3], Zonghang Liu[2], Philip C.Y. Chow[5], Zheng Zhao[2]*, Ryan T. K. Kwok[1], Jacky W. Y. Lam[1]*, Yucheng Liu[3]*, Shengzhong (Frank) Liu[3], and Ben Zhong Tang[1,2]*

1. *Department of Chemistry and Hong Kong Branch of Chinese National Engineering Research Center for Tissue Restoration and Reconstruction, The Hong Kong University of Science and Technology, Kowloon, Hong Kong, China.*

2. *School of Science and Engineering, Shenzhen Institute of Aggregate Science and Technology, The Chinese University of Hong Kong, Shenzhen (CUHK-Shenzhen), Guangdong 518172, China.*

3. *School of Materials Science and Engineering, Shaanxi Normal University, Xi'an 710119, China.*

4. *Department of Chemistry, Southern University of Science and Technology, Shenzhen 518055, China.*

5. *Department of Mechanical Engineering, The University of Hong Kong, Pokfulam 999077, Hong Kong, China.*

6. *These authors contributed equally: Chensen Li, Yaohui Li, Minghui Wu.*

Corresponding emails: zhaozheng@cuhk.edu.cn (Zheng Zhao); chjacky@ust.hk (Jacky W. Y. Lam); liuyc@snnu.edu.cn (Yucheng Liu); tangbenz@cuhk.edu.cn (Ben Zhong Tang)

Abstract: The design and fabrication of organic X-ray imaging scintillators with large Stokes shift, narrow-band, fast, and efficient radioluminescence becomes an attractive research direction in many fields, such as medical diagnostics, scientific instruments and high-energy physics. However, the trade-off between these diverse scintillation properties is an enormous challenge facing almost all scintillators. To overcome this limitation, in this work, we developed a strategy based on through-space heavy atom-π interactions to improve the performance of organic scintillators by introducing alkyl bromides into hybridized local and charge transfer (HLCT) emitters. Specifically, the HLCT state's locally excited characters result in a short radiative lifetime (3.74 ns) and

a narrow radioluminescence bandwidth (56 nm). The HLCT state's charge-transfer features yield a large Stokes shift (> 100 nm). Meanwhile, through-space bromine-π interactions enhance the photoluminescence quantum yield to 100%. Notably, a high X-ray imaging resolution (> 40.0 lp mm^{-1}) was achieved, making the highest spatial resolution for organic scintillators reported to date. This work provides a method to design scintillators with excellent comprehensive performances and paves the way towards promising applications for high-resolution X-ray imaging.

Introduction

Organic scintillators exhibit inherent advantages, such as abundant resources, high mechanical flexibility, easy processing, low cost and large-area fabrication, and have received much attention in recent years due to their potential applications in radiation detection, high-energy physics, medical radiography, security screening and astronomical discovery[1-6]. To develop efficient organic scintillators, some key parameters are required to be implemented, including (i) the short radiative lifetime (< 10 ns) enables quickly dynamic X-ray imaging and medical diagnosis[4]; (ii) the narrow full-width at half-maximum (FWHM) (< 60 nm) radioluminescence (RL) reduces scattering effects and improves the clarity and accuracy of imaging[7]; (iii) the large Stokes shift (> 100 nm) reduces self-absorption of X-ray sources and ensures the full utilization of excitation energy.[2-3]; and (iv) the high photoluminescence quantum efficiency (PLQY) (> 90%) is closely related to the high conversion efficiency of scintillators from X-ray to luminescence[2]. Traditional organic scintillators with strong absorption bands, such as anthracene[8], exhibit strong emission due to the large overlap of electron-hole wave functions in the singlet locally excited (LE) state (**Fig. 1a**). However, this excited-state character results in smaller Stokes shifts and lower utilization of triplet excitons. To circumvent these limitations, organic thermally activated delayed fluorescence (TADF)[9,10] scintillators with strong twisted intramolecular charge transfer[11] utilizing triplet excitons for RL emission have been

https://doi.org/10.26434/chemrxiv-2025-dhj18 ORCID: https://orcid.org/0009-0009-6810-7086 Content not peer-reviewed by ChemRxiv. **License:** CC BY 4.0

developed, which utilizes triplet excitons for RL emission (**Fig. 1a**). Apart from an increase in scintillation light production has been achieved, the radiative lifetimes are significantly extended to the microsecond time scale and the emission FWHMs are also expanded to 70~100 nm.

To solve the problems, the trade-off between LE and TADF with moderately twisted donor-acceptor structures can fully utilize their advantages and largely avoid their shortcomings (**Fig. 1a**). Therefore, organic scintillators with the character of hybridized local and charge transfer (HLCT)[12-14] excited state are highly promising candidates to promote the overall scintillation performance. HLCT scintillators[15] possess two combined and compatible characteristics: a LE state with a large oscillator strength and a charge transfer (CT) state with enhanced intersystem crossing (ISC) ability. Then the former one contributes to a high radiative rate and narrow emission spectrum, while the latter was responsible for the high triplet exciton utilization efficiency for the high-lying reversed ISC (hRISC) transition from upper triplet state (T_n) to singlet (S_1) state, which leads to high PLQYs. The weak binding of CT excitons can contribute to a large Stokes shift and narrow energy gap between S_1 and T_n (ΔE_{ST}), leading to a fast hRISC rate, which can intrinsically shorten the scintillation lifetime. These advantages can make HLCT scintillators perform well in RL detection and imaging.

However, the low X-ray absorption cross-section and subsequently poor detection sensitivity of organic scintillators due to their limited effective atomic numbers have substantially impeded their applications. Introduction of halogen heavy atoms (Cl, Br, and I) into scintillators are effective methods to significantly increase their X-ray absorption cross-section, X-ray sensitivity, and imaging resolution[3-4]. Nevertheless, traditional through-bond conjugated connections between halogen heavy atoms and emitters generally facilitate the (R)ISC process but enhance the nonradiative decay rate, which quenches their luminescence to result in low PLQYs (**Fig. 1b**). Consequently, the search for an appropriate molecular engineering approach to retain or enhance the

3

84 RL properties with introducing heavy atoms is of great importance to generate new

85 high-performance organic scintillators.

86
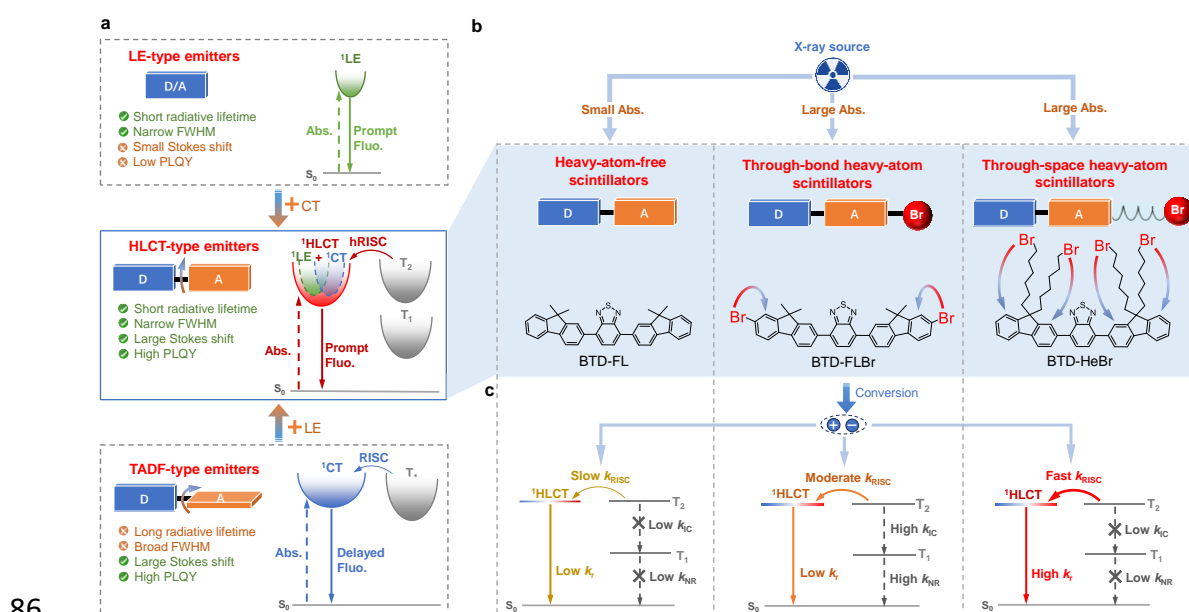
Fig. 1 | Illustration of the through-space heavy-atom strategy of HLCT scintillators

on the enhancement of X-ray performances. a, The three types of organic

scintillators with different CT characters. **b**, The three types of HLCT scintillators

(BTD-FL, BTD-FLBr, and BTD-HeBr) with different heavy atom strategies. **c**,

Mechanism by which the RL efficiency of HLCT scintillators is highly enhanced, which

occurs due to the enhanced X-ray absorption of heavy elements and their RISC

processes and minimized non-radiative decay. D, donor; A, acceptor; Abs., absorption;

Fluo., fluorescence; ^{1}CT, charge transfer singlet state; ^{1}LE, localized excited sate;

^{1}HLCT, hybridized local and charge transfer state; (h)RISC, (high-lying) reversed

intersystem crossing; TADF, thermally activated delayed fluorescence; T_1, the first

triplet state; T_2, the second triplet state; k_{RISC}, RISC rate; k_r, radiative transition rate; k_{IC},

internal conversion rate; k_{NR}, non-radiative transition rate.

99

Here, we proposed a novel concept for designing organic scintillators based on

nonconjugated alkyl bromide, in which heavy atom-π interactions[16-21] penetrate the

space between scintillators and heavy atoms, promoting the spin-orbital coupling (SOC)

4

103   between single and triplet states without increasing nonradiative decay (**Fig. 1b,c**). In

104   this motif, emitters and heavy atoms are spatially separated, but meanwhile allowing

105   external, rather than the internal heavy atom effect to occur. This concept has the

106   following advantages. Firstly, the emitters and heavy atoms can interact with each other

107   through spatial interactions to enhance the X-ray absorption cross-section. Secondly,

108   the spatial separation of emitters and heavy atom units will promote SOC between

109   singlet and triplet states, which can facilitate the (R)ISC process and increase the

110   exciton utilization efficiency. Thirdly, the nonconjugated architecture avoids the strong

111   nonradiative decay of singlet excitons resulted from the heavy atoms. Therefore,

112   considerable PLQY can be expected. As a result, the optimal balance among large

113   Stokes shift (> 100 nm), high PLQY (100%) and short decay time (3.74 ns) of organic

114   scintillation materials can be achieved simultaneously by HLCT emitters with attaching

115   through-space bromines. In this work, an X-ray scintillator named BTD-HeBr was

116   designed and prepared. It exhibits a narrow RL spectrum with FWHM of 56 nm, high

117   light yield of approximately 42,400 photons MeV^{-1} and a low detection limit of 84.6

118   nGy s^{-1}. More importantly, a high X-ray imaging resolution of > 40.0 line pairs per

119   millimeter (lp mm^{-1}) was achieved, which is the highest value for organic scintillators

120   reported so far. This finding provides a powerful design approach and promising new

121   alternative materials for fabricating organic X-ray imaging scintillators with

122   outstanding sensitivity, low cost and high stability using through-space heavy atom-π

123   interactions involving HLCT emitters.

124

125   **Photophysical properties**

126   BTD-FL[22] was selected as the preferred HLCT system due to its moderate dihedral

127   angle and appropriate donor [9,9-dimethyl-9H-fluoren (FL)] and acceptor

128   [benzothiadiazole (BTD)] strength, which exhibits partial HOMO–LUMO separations

129   and distinct HLCT characters (**Fig. 1b**). Introducing bromine atoms into BTD-FL to

130   improve SOC and absorption cross-section, resulting in BTD-FLBr. To minimized non-

5

131 radiative decay, the nonconjugated alkyl bromides were introduced into BTD-FL to

132 obtain BTD-HeBr. These three HLCT emitters can be easily synthesized by one-pot

133 method with a high reaction yield under the same reaction conditions by using different

134 substituted reactants (**Supplementary Fig. 1-8**).

135 The three abovementioned HLCT emitters showed similar absorption bands in the

136 ultraviolet and blue spectral ranges in dilute toluene solutions. A broad, featureless

137 absorption band was observed at around 360-500 nm with peak at 410 ~ 413 nm, which

138 is assigned to the intramolecular charge transfer (ICT) absorption associated with the

139 electron transfer from the fluorene to benzothiadiazole (**Fig. 2a**). Noteworthily, the

140 molar absorption coefficient ($\varepsilon > 2 \times 10^4$ L·mol^{-1}cm^{-1}) are significantly higher than

141 those of TADF emitters with TICT characters[23]. In contrast, the steady-state

142 photoluminescence (PL) spectra of these HLCT emitters show an unstructured emission

143 band from 480 to 640 nm centered at approximately 520 nm. Thanks to the CT character

144 of HLCT state, the overlaps between the absorption and emission spectra are small (free

145 reabsorption feature). This results in large Stokes shift (>100 nm), which is a

146 prerequisite for high-performance scintillators.

147 The solvatochromic test results to verify their HLCT characters are shown in **Fig. 2b,**

148 **c, &d**. When changing the solvent from low-polar hexane to the high-polar acetonitrile,

149 the UV-vis absorption spectra (**Supplementary Fig.9**) of the three HLCT emitters

150 remain virtually unchanged in terms of shape and position. This infers that the ground-

151 state dipole moment of the molecule is slightly affected by the solvent variation. In

152 contrast, the PL spectrum (**Fig. 2c**) of BTD-HeBr, for example, showed red-shifts by

153 40 nm from 508 to 548 nm accompanied with increasing spectrum broadness when the

154 solvent polarity becomes higher, indicating that the excited states possess certain CT

155 components. Particularly, the maximum PL peaks in low-polar solvents are almost

156 observed at the similar wavelengths, which is assigned to a LE-like character of the

157 singlet state. However, larger shift in PL maximum apparently occurs in the high polar-

158 solvents due to the formation of CT excited state. Therefore, BTD-HeBr contains both

6

159 the intrinsic LE and CT excited states and demonstrates HLCT characteristics. Besides,

160 the Stokes shifts ($v_a - v_f$) are calculated from absorption and emission spectra and are

161 plotted as a function of solvent polarity function (f) corresponding to the Lipper-Mataga

162 model to define the interactions between the solvent and dipole moment of the emitters

163 (**Fig. 2d**). The Lippert–Mataga plots show a two-section line corresponding to two

164 different exciton states with two distinguishable small and large dipole moments in low-

165 polar solvents ($f \leq 0.15$) and high-polar solvents ($f \geq 0.15$), respectively. In the high-

166 polarity region, the excited-state dipole moment (μ_e) was 18.4 D, which was close to

167 those of typical CT molecule 4-(N,N-dimethylamino)benzonitrile ($\mu_e = 23$ D)[24]. This

168 suggests a CT state-dominated character in high-polarity solvents. Besides, in the low-

169 polarity region, the μ_e value was 7.30 D, which is close to those of common LE

170 fluorophores such as anthracene (4.0–6.0 D)[25]. This provides strong evidence that

171 nonequivalent hybridization occurs between LE and CT initial states in BTD-HeBr,

172 which forms LE-based HLCT state in low-polar solvents and CT-dominated HLCT

173 state in high-polar solvents. Additionally, transient PL decay spectra of BTD-HeBr in

174 solvents of different polarities show single exponential decays within nanosecond range

175 of 3 ~ 5 ns (**Fig. 2d**), signifying that the excited-state responsible for the PL emission

176 originates from the hybridization between LE and CT excited states (HLCT state), not

177 a simple mix-up of the two states. The similar HLCT properties of BTD-FL and BTD-

178 FL are shown in **Supplementary Fig. 9-12** and **Supplementary Table 1**.

179   To understand in depth the photophysical properties, we studied the transient

180 spectroscopy (TA) spectra and dynamic trace of BTD-HeBr in tetrahydrofuran, as

181 shown in **Fig. 2e,f**. The positive band from 500 to 600 nm corresponds to stimulated

182 emission (SE), while the negative band from 650 to 730 nm was attributed to the

183 excited-state absorption (ESA). The proposed mechanism of transient component

184 evolution is shown in **Fig. 2g and Supplementary Fig. 13**. The initial distinct vibronic

185 SE band exhibits structured double peaks at 540 and 573 nm, associated with the LE-

186 dominated HLCT state. Later, it blue-shifts to 541 nm and becomes structureless due to

https://doi.org/10.26434/chemrxiv-2025-dhj18 ORCID: https://orcid.org/0009-0009-6810-7086 Content not peer-reviewed by ChemRxiv. **License:** CC BY 4.0

the vibrational cooling coupled planarization process[26], corresponding to the CT-dominated HLCT state. It is inferred that a quick equilibrium exists between the LE and CT parts of the HLCT state. The equilibrium constant K is estimated from $K = k_1/k_2 = \tau_2/\tau_1 = 1.37$, which means that the CT component is more pronounced than the LE component in the HLCT state. Over longer time delays, moderate spectral red shift to 558 nm with a monotonous decay in intensity was observed, which implies that LE and CT states undergo interstate coupling forming a HLCT emissive state. In addition, the third component (HLCT') was attributed to the solvent reorganization process from the HLCT state to the HLCT' state ($\tau_3 = 221$ ps), and the subsequent time constant $\tau_4 = 3239$ ps was attributed to the decay from the HLCT' state to the ground state.
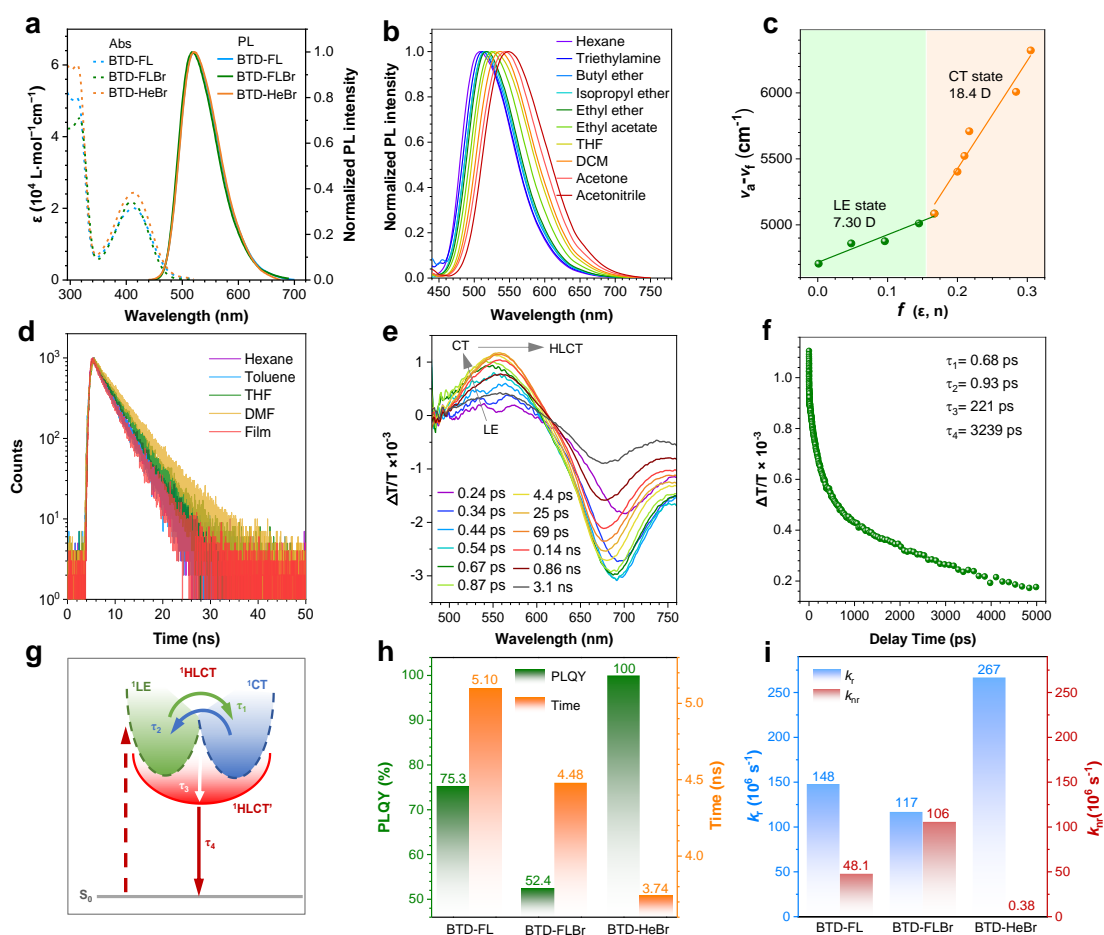
Fig. 2 | Photophysical properties of the HLCT emitters in solution and neat films.
a, UV-vis and PL spectra of BTD-FL, BTD-FLBr, and BTD-HeBr in toluene solutions (10^{-5} M). **b**, PL spectra of BTD-HeBr in different solvents with vary polarity. **c**, Linear

201 correlation of orientation polarization (f) of solvent media with the Stokes shift ($v_a - v_f$)

202 for BTD-HeBr. **d**, Transient PL decay spectra of BTD-HeBr in different solvents and

203 neat films. **e**, Time-resolved transient absorption spectra of BTD-HeBr in

204 tetrahydrofuran solutions. **f**, Transient absorption dynamic trace at 550 nm. **g**, Proposed

205 excited-state deactivation mechanism of BTD-HeBr. **h**, PLQYs and PL decay lifetimes

206 of BTD-FL, BTD-FLBr, and BTD-HeBr in neat films. **i**, Radiative transition rate (k_r)

207 and nonradiative transition rate (k_{nr}) of BTD-FL, BTD-FLBr, and BTD-HeBr in neat

208 films.

209

210   The photophysical properties of the emitters in the aggregate state are crucial for

211 high-sensitive X-ray detection and imaging applications. The curves of PL intensity in

212 water/THF mixtures with different water fractions proves that the three HLCT

213 molecules show aggregation-induced emission (AIE) characteristics[27-28]

214 (**Supplementary Fig. 14)**, which can demonstrate potential performance as X-ray

215 scintillators. The development of scintillators with higher efficiency and faster timing

216 properties is always the primary aim of this field. The key to achieving intrinsic efficient

217 and fast organic scintillators is to eliminate the occupation of T_1 states without any loss

218 of the utilization efficiency of triplet excitons. As expected, the fluorescence lifetime

219 decreases from 5.10 ns for BTD-FL to 4.48 ns for BTD-FLBr due to the increased SOC

220 and (R)ISC processes by introducing bromine atoms. Notably, the fluorescence lifetime

221 further decreases to 3.74 ns in BTD-HeBr, showing that through-space bromine atoms

222 can significantly enhance the (R)ISC processes due to the numerous spatial interactions

223 between bromine atoms and emitters in the aggregate state (**Fig. 2h and**

224 **Supplementary Fig. 15**). In addition, due to the efficient hRISC processes between the

225 triplet and singlet states, the BTD-FL exhibits a high PLQY of 75.3% in neat film

226 (**Supplementary Fig. 16**). In contrast, the direct connection of bromine lead to largely

227 fluorescence quenching in BTD-FLBr because of the enhanced non-radiative decay rate

228 of the triplet states. Therefore, BTD-FLBr with through-bonded bromines only exhibits

9

229   a relatively low PLQY of 52.4%, which is disadvantageous to achieve highly efficient

230   X-ray detection. However, the nonconjugated alkyl chains with through-space bromine

231   atoms in BTD-HeBr not only enhance the (R)ISC processes but also significantly

232   suppress the non-radiative decays of the triplet states. The detailed discussions will be

233   given in the next part. As a result, the PLQY of BTD-HeBr is largely increased to 100%,

234   implying a promising organic scintillation performance. To more accurately ascertain

235   the changes in the photophysical processes, we calculated the radiative transition rate

236   (k_r), and nonradiative transition rate (k_{nr}) of the three emitters **(Fig. 2i)**. According to

237   the formulas[29] $k_r = \Phi_f/\tau$ and $k_{nr} = 1/\tau - k_r$ (where Φ_f represents the PLQY and τ is the

238   PL decay lifetime), the k_r of 1.48×10^8 s^{-1} in BTD-FL slightly decreases to 1.17×10^8 s^{-1}

239   in BTD-FLBr but largely increases to 2.67×10^8 s^{-1} in BTD-HeBr, which indicates that

240   a short fluorescence lifetime and a high PLQY value can greatly facilitate the singlet

241   radiative transition process. On the other hand, in comparison with the relative lower

242   k_{nr} of BTD-FL (4.81×10^7 s^{-1}), the k_{nr} of BTD-FLBr (1.06×10^8 s^{-1}) is obviously higher,

243   due to the fluorescence quenching by through-bond bromine atoms. In contrast, the

244   even lower k_{nr} of BTD-HeBr (3.80×10^5 s^{-1}) indicates the little effect of through-space

245   bromines on fluorescence quenching. It is found that BTD-HeBr with through-space

246   bromine atoms not only largely improves the radiative rate, but also dramatically

247   suppresses the non-radiative decay rate, which are beneficial for achieving high-

248   sensitive X-ray detection.

249

Theoretical calculations

251   To examine the excited states of the HLCT emitters, theoretical calculations are

252   conducted by exploiting the density functional theory (DFT) and time-dependent DFT

253   (PBE0/6-31g(d,p)).[30,31] The frontier orbital distributions of the ground states of the

254   three emitters display typical HLCT characters **(Supplementary Fig. 17)**. In the S_1 state,

255   the molecular geometry of BTD-HeBr displays weak C-H⋯N interactions (2.45 Å) and

256   C-H⋯π interactions (2.28 Å) between the BTD acceptors and the fluorene donors. Such

10

257   spatial interactions create weak steric hindrance, resulting in a moderate dihedral angle

258   of 36.3° between the two units. Therefore, the HLCT state of BTD-HeBr with a

259   moderate ICT character was expected. Natural transition orbital (NTO) analyses[32-33] are

260   also performed to explore the excited states and transition characters (**Fig. 3a**). The hole

261   of S_1 was mostly distributed on the whole conjugated system, while the electron was

262   mainly located on the BTD acceptor. In detail, the hole and electron delocalization

263   indexes (HDI & EDI) are 4.57 and 7.91, respectively, indicating the higher the degree

264   of delocalization of holes and the greater spread of their distribution than that of

265   electron. Therefore, the S_1 presents a hybrid feature of LE (43.8%) and CT (57.2%). To

266   further verify the excited-state characters, the distributions of hole and electron in BTD

267   and fluorene fragments as heat maps are shown in **Fig. 3b**. In BTD, the electron

268   composition was significantly higher at 86.2% and the hole composition was 28.8%.

269   This unit results in a 49.8% overlap and demonstrates a typical HLCT feature. In

270   contrast, the fluorene exhibits a main hole composition of 70.9%, an electron

271   composition of 13.5%, and an overlap of 30.9%, which can be considered to show CT

272   feature. These results illustrate that the HLCT features of BTD-HeBr mainly come from

273   the BTD acceptors. In addition, the S_1 states of BTD-FL and BTD-FLBr show similar

274   HLCT features (**Supplementary Fig. 18-20)**. The HLCT characteristics are beneficial

275   for the luminescence transition and utilization of excited excitons. Specifically, the LE

276   character of ^{1}HLCT state of the three HLCT emitters renders a high oscillator strength

277   (f = 0.554–0.679) from S_1 to S_0. Due to the higher T_n of the emitters are LE-dominated

278   states (**Supplementary Fig. 21-23)** according to EI-Sayed rule[34], the CT character of

279   ^{1}HLCT states results in a high SOC constant (0.53–0.74 cm^{-1}) between S_1 and T_n, which

280   is beneficial for a fast radiative transition and efficient (R)ISC processes.

281   In further calculations, the energy-level arrangements of BTD-FL, BTD-FLBr, and

282   BTD-HeBr are studied (**Fig. 3c and Supplementary Fig. 24)**. The excited state levels

283   of the three HLCT emitters exhibit a tiny energy difference (0.02–0.03 eV) between S_1

284   and T_2. A small energy difference (0.06–0.11 eV) between S_1 and T_3 was also found,

11

which implies that the spin-flip routes from higher triplet ($T_{2,3}$) to singlet (S_1) states are feasible. Besides, a low energy level of T_1 (1.70 eV) and a large energy gap (0.95–1.00 eV) between T_1 and T_2 are observed, which can effectively suppress interconversion (IC) transition between them. The energy levels of the molecules can be identified from their prompt and delayed PL spectra at low temperature (**Supplementary Fig. 25)**.
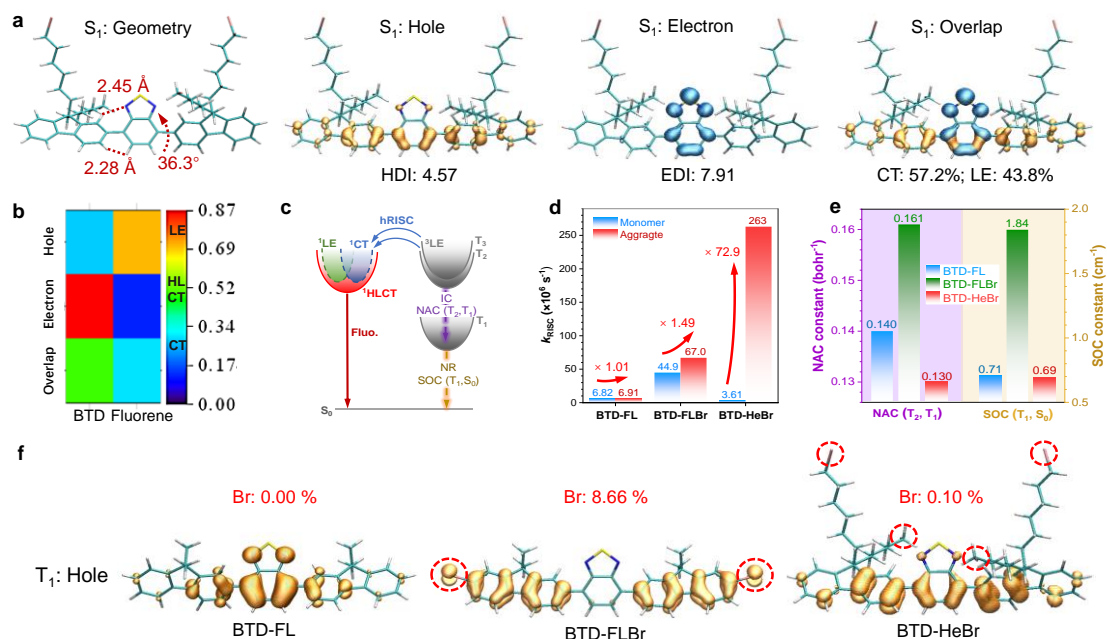
Fig. 3 | Theoretical calculations of the excited states for the HLCT emitters. a, the optimized geometry structures, hole distributions, electron distributions, and hole-electron overlaps of S_1 of BTD-HeBr. **b**, The heat map of intramolecular fragment-fragment charge transfer matrix of S_1 of BTD-HeBr. **c**, Diagram of energy levels and properties of the excited states and the photophysical processes of BTD-HeBr. **d**, The RISC rates of BTD-FL, BTD-FLBr, and BTD-HeBr in monomer and aggregate state. **e**, The NAC constants between T_2 and T_1 and SOC constants between T_1 and S_0 of BTD-FL, BTD-FLBr, and BTD-HeBr in the aggregate state. **f**, The hole distributions of T_1 of BTD-FL, BTD-FLBr, and BTD-HeBr in the aggregate state. HDI: hole delocalization index; EDI: electron delocalization index; hRISC: high-lying reverse intersystem crossing; IC: interconversion; NAC: vibronic nonadiabatic coupling; SOC: spin-orbital coupling; k_{RISC}: rate constant of the RISC process.

304   Moreover, large SOC matrix elements are very important for improving the rate of

305   RISC processes[35] (**Fig. 3d** and **Supplementary Equation 1**). In the monomer state, the

306   constants of SOC (T_2, S_1) of three HLCT emitters are small (0.028–0.2 cm^{-1}) for all

307   molecules, implying a low possibility for the occurrence of the RISC process

308   (**Supplementary Fig. 26**). However, significantly higher values (0.53–0.74 cm^{-1}) are

309   observed for SOC (T_3, S_1), which triggers an efficient spin-flip occurring. Consequently,

310   the k_{RISC} values are calculated to be 3.61–44.9×10^6 s^{-1}, which are comparable to those

311   of efficient TADF emitters[36].

312   In the aggregate state, the SOC (T_2, S_1) and SOC (T_3, S_1) remain almost unchanged

313   (**Fig. 3d**), with a k_{RISC} of ~6.9×10^6 from monomer to aggregate states, that was slightly

314   increased by 1.01 times. Compare with monomer, BTD-FLBr with directed connected

315   bromine atoms in the aggregate state displays obviously larger SOC (T_2, S_1) and SOC

316   (T_3, S_1) of 1.30 and 0.86 cm^{-1}, respectively, leading to dual effective RISC channels (T_2

317   →S_1 and T_3→S_1). Therefore, the k_{RISC} increases by 1.49 folds, reaching 6.70 × 10^7 s^{-1}

318   due to the more spatial interactions between bromine atoms and π-electrons

319   (**Supplementary Fig. 27**). For BTD-HeBr, the SOC (T_2, S_1) was dramatically increased

320   from 0.045 to 1.87 cm^{-1}, and the SOC (T_3, S_1) also surges from 0.53 to 0.95 cm^{-1} in the

321   aggerate state. This results in a significant ~73-fold increase in RISC rate (k_{RISC}=2.63

322   × 10^8 s^{-1}) with dual efficient RISC channels. These results indicate that aggregation

323   greatly promotes the RISC process through external heavy atom effects by introducing

324   through-space bromine atoms (**Supplementary Fig. 28**), enables BTD-HeBr to exhibit

325   excellent X-ray scintillation performance.

326   Apart from efficient RISC process, a low nonradiative decay of HLCT emitters is

327   also significant factor for achieving efficient X-ray detection. As illustrated in **Fig. 3e**,

328   the vibronic nonadiabatic coupling (NAC) matrix element between T_1 and T_2 states can

329   be calculated to further evaluate the possibility of the existence of the IC process. The

330   k_{IC}(T_2→T_1) was calculated by using the following equation[37]:

331    $$k_{IC}(T_2 \rightarrow T_1) \propto \left| \frac{\langle NAC(T_2, T_1) \rangle}{E(T_2) - E(T_1)} \right|^2 \tag{1}$$

13

332   where $\langle NAC(T_2, T_1)\rangle$ is the NAC matrix between T_2 and T_1, $E(T_2)/E(T_1)$ is the

333 energy level of T_2/T_1. The calculated root-mean-square (RMS) NACs are 0.140, 0.161

334 and 0.130 bohr^{-1} for BTD-FL, BTD-FLBr and BTD-HeBr, respectively. BTD-FLBr

335 displays the largest NAC (T_2, T_1), which suggests that introducing directed connected

336 bromine atoms increase the IC process and is unfavorable to efficient luminescence.

337 Owing to smallest NAC, the IC process between T_1 and T_2 of BTD-HeBr is least likely

338 to exchange the exciton populations between them. The difference of NACs probably

339 due to the difference of contribution of bromine to the excited state wave function[17-20].

340 For BTD-FLBr, the contribution of bromine atoms to hole distribution in T_1 and T_2 is

341 as high as 8.66% and 8.26%, respectively (**Fig. 3f and Supplementary Fig. 22,23&29**).

342 In contrast, these values of BTD-HeBr in T_1 and T_2 is as low as 0.10% and 0.00%,

343 respectively. These results indicate that the contribution of the excited state wave

344 function of bromine is greatly reduced through the spatial heavy atom strategy, resulting

345 to distinctly low nonradiative decay. In addition, the non-radiative transition from T_1 to

346 S_0 is another important deactivation route of the triplet exciton. The $k_{nr}(T_1 \rightarrow S_0)$ was

347 calculated using the following equation[38]:

348     $$k_{nr}(T_1 \rightarrow S_0) \propto \frac{\langle SOC(T_1, S_0)\rangle^2}{\{E(T_1) - E(S_0)\}^2 + \gamma^2} \tag{2}$$

349   where $\langle SOC(T_1, S_0)\rangle$ is the SOC matrix between T_1 and S_0, γ is the broadening of

350 the line-shape function for ISC (**Fig. 3e**). The SOC (T_1, S_0) of 0.71 cm^{-1} in BTD-FL

351 increases significantly to 1.84 cm^{-1} in BTD-FLBr due to the partial hole distribution

352 from direct-linked bromine to T_1, which triggers a much stronger nonradiative decay

353 (**Fig. 3f and Supplementary Fig. 29**). However, the SOC (T_1, S_0) of BTD-HeBr not

354 increases but decreases slightly to 0.69 cm^{-1}, displaying such through-space heavy atom

355 strategy can effectively suppress triplet nonradiative decay to achieve efficient X-ray

356 detection and imaging.

357

358 **Radioluminescence properties**

359　　　X-ray absorption measurements of BTD-FL, BTD-FLBr, and BTD-HeBr are

360　　performed to investigate their X-ray absorption ability (**Fig. 4a**). As expected, the

361　　resonant absorption edges largely increase from BTD-FL to BTD-FLBr and BTD-HeBr

362　　due to the introduction of heavy atoms. The absorption coefficients of BTD-HeBr (Z_{max}

363　　= 35, K_α = 13.5 keV) was slightly higher than that of BTD-FLBr, which indicates that

364　　the through-space bromine atoms exhibit better X-ray photon absorption ability.

365　　Moreover, the attenuation efficiency (**Supplementary Fig. 30)** of BTD-FL, BTD-FLBr,

366　　and BTD-HeBr was calculated to be 18.7 and 69.3 and 75.1% at a thickness of 10 mm,

367　　respectively. In a further set of experiments, we explored the RL behaviors of the HLCT

368　　emitters in the solid state (**Fig. 4b,c**). Under the same X-ray irradiation (dose rate, 2.023

369　　mGy s^{-1}), BTD-FL and BTD-FLBr display weak X-ray emission, which is not

370　　obviously observable by the naked eye owing to their weak X-ray absorption or low

371　　PLQY.[39] In contrast, BTD-HeBr exhibits clearly brighter yellow X-ray luminescence

372　　with a narrow FWHM of 56 nm under a continuous X-ray source, which is considerably

373　　narrower than that of commercial inorganic scintillators such as CsI:Tl, PbWO$_4$,

374　　YAlO$_3$:Ce, and Bi$_4$Ge$_3$O$_{12}$.[5] This narrow FWHM can be attributed to the LE character

375　　of the HLCT state. Therefore, the much higher radioluminescence intensity of BTD-

376　　HeBr reveals the through-space heavy atom strategy are highly successful for designing

377　　bright X-ray scintillators. A comparison with standard scintillators shows that BTD-

378　　HeBr exhibited high relative light yield of ~42,400 photons MeV^{-1} (dose rate, 2.023

379　　mGy s^{-1}) (**Supplementary Fig. 31**). The high relative light yield of BTD-HeBr is

380　　mainly due to their high X-ray absorption cross-section, unit exciton utilization

381　　efficiency and low non-radiative decay. In addition, BTD-HeBr films exhibits good

382　　photostability (**Fig. 4d**). Specifically, when BTD-HeBr was exposed to a high dose rate

383　　of X-ray (2.023 mGy s^{-1}) for a continuous 10 h, the RL intensity remains at around 98%

384　　of the initial value, which is comparable with that of commercial plastic scintillators[1].

385　　Moreover, the emission intensity of BTD-HeBr remains > 96% under repeated X-ray

386　　excitation for 50 min (57 on–off circles), highlighting its good photostability. In

15

387   addition, the average luminescence decay time of BTD-HeBr (excited using an X-ray

388   pulse) is fitted as 3.43 ns (**Supplementary Fig. 32**), which is consistent with the PL

389   decay time (3.74 ns). Furthermore, the RL intensity of BTD-HeBr was linear response

390   to the X-ray dose rate in the range $0.401-570.1$ µGy s^{-1} (**Fig. 4e,f**). Additionally, the

391   detection limit is a measure of the response linearity at low excitation levels and can be

392   defined as the dose rate at which the signal-to-noise ratio (SNR) equals 3. The detection

393   limit was 84.6 nGy s^{-1} for BTD-HeBr films, which is significantly below the minimum

394   X-ray dose rate requirement for medical X-ray imaging (5.5 µGy s^{-1})[40], demonstrating

395   the highly potential of medical radiography applications.

396
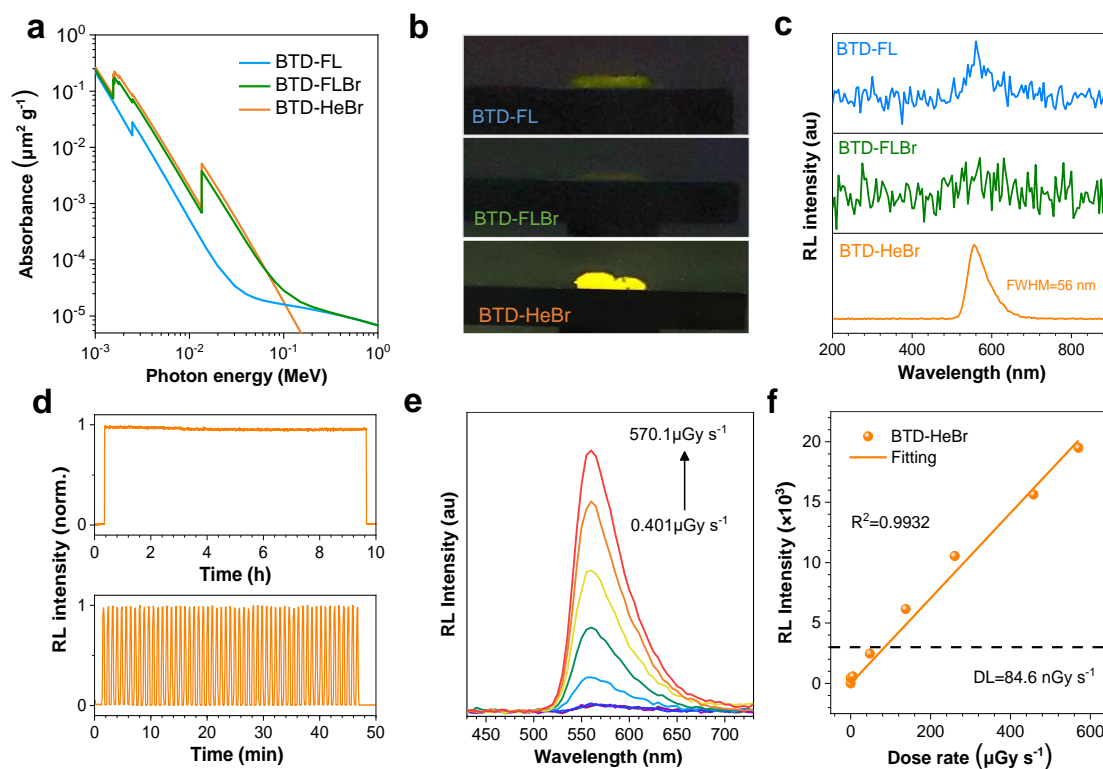
Fig. 4 | RL performance characterizations of the HLCT scintillators. a, X-ray absorption spectra of BTD-FL, BTD-FLBr, and BTD-HeBr emitters measured as a function of X-ray energy[41]. **b**, Images of these HLCT emitters taken under X-ray irradiation (X-ray tube voltage, 50 kV; dose rate, 2.023 mGy s^{-1}). **c**, RL spectra of these HLCT emitters with an optimal thickness (X-ray tube voltage, 50 kV; dose rate, 2.023 mGy s^{-1}). **d**, The RL emission photostability for the BTD-HeBr versus continuous irradiation (top) and repeated on–off cycles of X-rays (bottom) at a dose rate of 2.023

mGy s^{-1}. **e**, The RL spectra of BTD-HeBr measured at different X-ray dose rate ranging from 0.401 to 570.1 μGy s^{-1}. **f**, The linear relation between X-ray dose rate and RL intensity and detection limit of BTD-HeBr.

To achieve high performance and good processability of the HLCT scintillation films for X-ray imaging, glassy neat films are fabricated by melting the HLCT emitters at a relatively low temperature of 120°C for X-ray correlated measurements due to their low glass transition temperatures (**Supplementary Fig. 33**). The thickness-dependent RL of BTD-HeBr shows significantly high intensity with an optimal thickness at 180 μm (**Supplementary Fig. 34**). In addition, the transmittance of the BTD-HeBr glassy film exceeds 93% within the wavelength range of 500–800 nm, encompassing the entire emission spectrum (**Supplementary Fig. 35**). This feature can enhance the photon collection efficiency during optical characterization and may realize high resolution for X-ray imaging. The ultra-high X-ray imaging resolution of 40.5 lp mm^{-1} was achieved at a modulation transfer function (MTF) of 0.2 for BTD-HeBr scintillation screen, according to the MTF calculation of standard X-ray edge images[42] (**Fig. 5a**). As far as we know, such a high imaging resolution exceeds those of all reported organic scintillators (**Fig. 5b** and **Supplementary Table 2**), which supports the high practical potential of using through-space heavy atom-π interactions for efficient X-ray imaging scintillators in HLCT emitters. To further verify this value, we took X-ray images of a standard X-ray test pattern plate. A bright-field photograph was shown in **Supplementary Fig. 36**, and the X-ray image (**Fig. 5c**) demonstrates that the line pair notches at 33.3 lp mm^{-1} were clearly detectable and the line pair notches at 50.0 lp mm^{-1} were roughly detectable. Furthermore, we performed imaging tests using BTD-HeBr scintillators to demonstrate their practical value. Spring-loaded pens, positioned between an X-ray source and a BTD-HeBr film (**Figure 5d**), allowed the otherwise invisible springs to be distinctly captured on the film, with the plastic casing appearing almost transparent. Furthermore, X-ray contrast imaging facilitated the examination of

432 the intricate internal structure of an electronic chip, which is typically impenetrable to

433 the naked eye (**Figure 5e**). The intricate architecture of the electronic chip was vividly

434 revealed using a BTD-HeBr scintillating screen. These results demonstrate the

435 promising potential of the HLCT scintillators with through-space heavy atom-π

436 interactions in medical radiography.
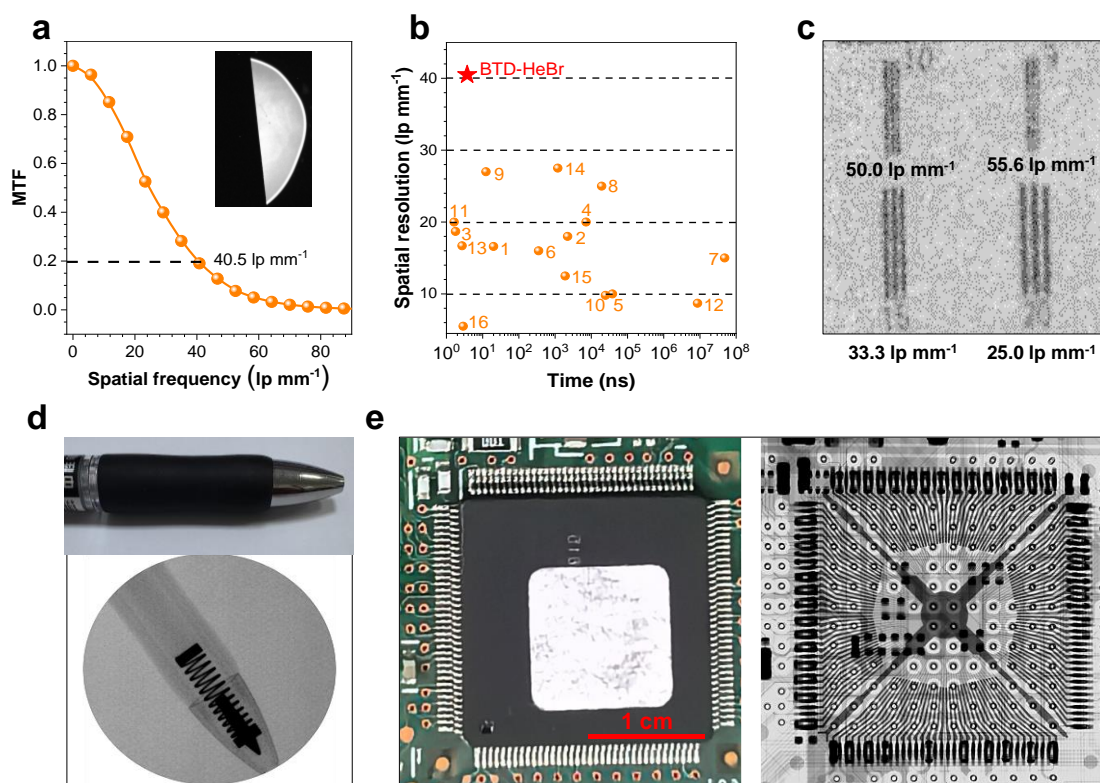
437

438 **Fig. 5 | Highly resolved X-ray imaging based on the HLCT scintillators. a**,

439 Modulation transfer function (MTF) of an X-ray slanted-edge image (inset) reveals a

440 spatial resolution of 40.5 lp mm^{-1} for BTD-HeBr screen. **b**, Comparison of scintillator

441 spatial resolution and lifetime of glassy BTD-HeBr film and previously reported

442 organic scintillators. **c**, X-ray image of a partial region (from 25.0 to 55.6 lp mm^{-1}) of

443 the standard X-ray test pattern plate. **d,e** Bright- and darkfield photographs of a pen (**d**)

444 and an electronic chip (**e**) before and after X-ray exposure (dose rate, 2.023 mGy s^{-1}).

445

446 **Conclusion**

447   In this work, we have developed a new strategy of organic scintillators to achieve

448 excellent comprehensive performance of RL. This kind of scintillators overcomes the

18

449   intrinsic shortcomings of LE-type and TADF-type scintillators to achieve fast radiative

450   lifetime, narrow FWHM, large Stokes shift, and high PLQY simultaneously.

451   Additionally, we developed a novel strategy based on through-space heavy atom-π

452   interactions for chemically modifying HLCT emitters. Thanks to the numerous spatial

453   interactions between bromine atoms and π-electrons, BTD-HeBr shows short radiative

454   lifetime (3.74 ns), high PLQY (100%), RISC rate (2.63×10^8 s^{-1}), small nonradiative

455   decay (3.8×10^5 s^{-1}) and X-ray absorption cross-section in the aggregate state. The

456   through-space-heavy-atom HLCT scintillators exhibit highly improved scintillation

457   performance (light yield of ~42,400 photons MeV^{-1}, narrow FWHM of 56 nm, and

458   detection limit of 84.6 nGy s^{-1}). In addition, a transparent screen can be obtained by

459   melting glassy films of BTD-HeBr to obtain ultrahigh X-ray imaging resolution of >

460   40.0 lp mm^{-1}, exceeding the resolution of all the reported organic and commercial

461   scintillators. We believe that the present findings will serve as a benchmark for the

462   fabrication of efficient organic scintillators in real-life applications, including medical

463   and security screening from materials beyond high-cost metal complexes and

464   perovskites[43-45] by using a simple through-space-heavy-atom strategy on HLCT

465   emitters.

466

Method

467

Materials

468

469   Unless otherwise noted, all the chemicals and reagents were obtained from commercial

470   sources (J&K, TCI, Meryer or Sigma Aldrich). The solvents for reactions were distilled

471   and degassed before use. All reactions were carried out in an N_2 atmosphere with a

472   dried Schlenk glassware or tube. ^{1}H and ^{13}C nuclear magnetic resonance (NMR) spectra

473   were measured using deuterated $CDCl_3$ as solvent on a Bruker AV 500 spectrometer or

474   a Bruker AVIII 400 spectrometer at room temperature. High-resolution mass spectra

475   (HRMS) were obtained on a GCT premier CAB048 mass spectrometer.

Characterization

476

UV-Vis absorption spectra were measured on a PerkinElmer Lambda 950 spectrophotometer. Photoluminescence (PL) spectra, transient PL decay spectra and photoluminescence quantum yields were performed on an Edinburgh FLS1000 fluorescence spectrofluorometer. Thermogravimetric analysis (TGA) was carried out on TA TGA Q5000 under dry nitrogen at a heating rate of 10 °C min^{-1}. Thermal transition was investigated by TA DSC Q1000 under dry nitrogen at a heating rate of 10 °C min^{-1}. Transient absorption spectroscopy (TAS) is conducted using an Ultrafast Systems Helios femtosecond transient absorption spectrometer. A femtosecond laser amplifier from Light Conversion generates a series of 1030 nm pulses, which are then divided into two separate beams to create the pump and probe pulses. For the probe, the pulses are focused onto a sapphire crystal and a YAG crystal, producing a visible (500-910 nm) and infrared (1100-1600 nm) continuum, respectively. To generate the pump beam centered at 400 nm, an optical parametric amplifier is used. A mechanical delay stage controls the time delay between the pump and probe pulses, ensuring precise measurements.

Computational Details

The ground state geometries were optimized using the density functional theory (DFT) method with PBE0-D3 functional at the basis set level of 6-31G (d, p), and the excited-state geometries were optimized using the time-dependent DFT method with PBE0-D3 functional at the basis set level of 6-31G (d, p). The above calculations were performed using Gaussian16 package. The spin-orbital coupling and non-adiabatic coupling constants were calculated based on PBE0/def2-SV(P) by using ORCA 5.0.2. The natural transition orbital analyses were analyzed with Multiwfn.

Fabrication of BTD-HeBr scintillation films

The scintillation films were prepared using a simple and conventional melt-quenched technique. 500 mg of BTD-HeBr was transferred to a beaker and heated at 120 °C until it melts and the bubbles disappear. Subsequently, the liquid in the beaker mentioned above was poured into a quartz plate, and the scintillation films with a thickness of

20

505   approximately 180 microns and a diameter over 2.5 cm were formed through rapidly

506   cooling at room temperature.

507   **X-ray detection performance and X-ray imaging measurements**

508   The radioluminescence was measured using a fluorescence spectrophotometer (Omni-

509   λ 300i, Zolix). For X-ray imaging measurement, a tungsten anode X-ray tube

510   (Hamamatsu Photonics, L11831-01) was used as the X-ray source. The X-ray tube

511   voltage was adjusted from 40 kV to 90 kV, and the current was adjusted from 10 μA to

512   200 μA to change the dose rate of the X-rays. The dose rate of X-rays was further fine-

513   modulated by changing the distance between the SC scintillator and the X-ray source.

514   The X-ray dose rate was cautiously calibrated using a Fluke Si diode (RaySafe X2)

515   dosimeter. The objects for imaging and the scintillators were placed perpendicular to

516   the incident X-rays, and the scintillator was integrated onto a commercial Si-

517   photodetector array to form the X-ray module (iRay, NDT0505J). All measurements

518   were taken at room temperature in air.

519

520   **Online content**

521   Any reporting summaries, source data, extended data, supplementary information,

522   acknowledgments, peer review information; details of author contributions and

523   competing interests, and statements of data and code availability are available at

524   https://doi.org/.

525

526   **Data availability**

527   All data are available in the main text and supplementary materials. The data and code

528   that support the findings of this study are available from the corresponding authors on

529   request.

530

531   **Author contributions**

532   C.L. designed the experiments and performed the synthesis, major theoretical

calculations, and photophysical measurements. Z. Z and B. Z. T supervised the project. Y.L. and B. J. performed X-ray imaging and detection measurements. M.W. performed photophysical measurements. F.K. performed transient absorption spectra measurements. Z.L. performed the partly theoretical calculations. P.C., Z.Z., R.K., J.L., Y.L., S.L., and B.Z.T. took part in the discussion and gave important suggestions. Y.L. and M.W. co-wrote the paper. All authors approved the final version of the manuscript.

Competing interests

The authors declare no competing interests.

Acknowledgements

Characterization and Preparation Center, The Chinese University of Hong Kong,

Shenzhen, for materials characterization.

References

1. Wang, X. *et al.* Organic phosphors with bright triplet excitons for efficient X-ray-excited luminescence. *Nat. Photon.* **15**, 187-192 (2021).

2. Ma, W. *et al.* Thermally activated delayed fluorescence (TADF) organic molecules for efficient X-ray scintillation and imaging. *Nat. Mater.* **21**, 210-216 (2021).

3. Wang, J.-X. *et al.* Heavy-atom engineering of thermally activated delayed fluorophores for high-performance X-ray imaging scintillators. *Nat. Photon.* **16**, 869-875 (2022).

4. Du, X. *et al.* Efficient and ultrafast organic scintillators by hot exciton manipulation. *Nat. Photon.* **18**, 162-169 (2024).

5. Chen, M. *et al.* Organic Semiconductor Single Crystals for X-ray Imaging. *Adv. Mater.* **33**, 2104749 (2021).

6. Yuan, J. W. *et al.* Highly Efficient Stable Luminescent Radical-Based X-ray Scintillator. *J. Am. Chem. Soc.* **145**, 27095-27102 (2023).

7. Zhou, W. *et al.* Sb-Doped Cs_3TbCl_6 Nanocrystals for Highly Efficient Narrow-Band Green Emission and X-Ray Imaging. *Adv. Mater.* **36**, e2302140 (2024).

8. Maddalena, F. et al. Inorganic, organic, and perovskite halides with nanotechnology for high–light yield X- and γ-ray scintillators. *Crystals* **9**, 88 (2019).

9. Uoyama, H., Goushi, K., Shizu, K., Nomura, H. & Adachi, C. Highly efficient organic light-emitting diodes from delayed fluorescence. *Nature* **492**, 234-238 (2012).

10. Liu, Y., Li, C., Ren, Z., Yan, S. & Bryce, M. R. All-organic thermally activated delayed fluorescence materials for organic light-emitting diodes. *Nat. Rev. Mater.* **3**, 1-20 (2018).

11. Wang, C. *et al.* Twisted intramolecular charge transfer (TICT) and twists beyond

TICT: from mechanisms to rational designs of bright and sensitive fluorophores. *Chem. Soc. Rev.* **50**, 12656-12678 (2021).

12. Li, W. *et al.* A Twisting Donor-Acceptor Molecule with an Intercrossed Excited State for Highly Efficient, Deep-Blue Electroluminescence. *Adv. Funct. Mater.* **22**, 2797-2803 (2012).

13. Xu, Y., Xu, P., Hu, D. & Ma, Y. Recent progress in hot exciton materials for organic light-emitting diodes. *Chem. Soc. Rev.* **50**, 1030-1069 (2021).

14. Wang, C. *et al.* Highly Efficient Nondoped Green Organic Light-Emitting Diodes with Combination of High Photoluminescence and High Exciton Utilization. *ACS Appl. Mater. Interfaces* **8**, 3041-3049 (2016).

15. Chandra, A., Turro, N., Lyons Jr, A. & Stone, P. The intramolecular external heavy atom effect in bromo-, benzo-, and naphthonorbornenes. *J. Am. Chem. Soc.* **100**, 4964-4968 (1978).

16. Rae, M., Fedorov, A. & Berberan-Santos, M. N. Fluorescence quenching with exponential distance dependence: Application to the external heavy-atom effect. *J. Chem. Phys.* **119**, 2223-2231 (2003).

17. Santos, M. N. B. External heavy-atom effect on fluorescence kinetics. *PhysChemComm* **3**, 18-23 (2000).

18. Shi, H. *et al.* Highly Efficient Ultralong Organic Phosphorescence through Intramolecular-Space Heavy-Atom Effect. *J. Phys. Chem. Lett.* **10**, 595-600 (2019).

19. Sun, X., Zhang, B., Li, X., Trindle, C. O. & Zhang, G. External Heavy-Atom Effect via Orbital Interactions Revealed by Single-Crystal X-ray Diffraction. *J. Phys. Chem. A* **120**, 5791-5797 (2016).

20. He, Y. *et al.* Highly Efficient Room-Temperature Phosphorescence Promoted via Intramolecular-Space Heavy-Atom Effect. *Adv. Opt. Mater.* **11**, 2201641 (2023).

21. Liu, J. *et al.* Experimental evidence for "hot exciton" thermally activated delayed fluorescence emitters. *Adv. Opt. Mater.* **7**, 1801190 (2019).

22. Zhang, Z. *et al.* Diarylethenes with a Narrow Singlet–Triplet Energy Gap Sensitizer:

24

617 a Simple Strategy for Efficient Visible-Light Photochromism. *Adv. Opt. Mater.* **6**,

618 1700847 (2018).

619 23. Grabowski, Z. R., Rotkiewicz, K., & Rettig, W. Structural Changes Accompanying

620 Intramolecular Electron Transfer: Focus on Twisted Intramolecular Charge-

621 Transfer States and Structures. *Chem. Rev.* **103**, 3899-4032 (2003).

622 24. Wan, Q. *et al.* Feasible structure-modification strategy for inhibiting aggregation-

623 caused quenching effect and constructing exciton conversion channels in acridone-

624 based emitters. *Phys. Chem. Chem. Phys.* **21**, 9837-9844 (2019).

625 25. Zhang, W. *et al.* Solvation-Dependent Excited-State Dynamics of Donor–Acceptor

626 Molecules with Hybridized Local and Charge Transfer Character. *J. Phys. Chem.*

627 *C* **124**, 5574-5582 (2020).

628 26. Zhao, Z., Zhang, H., Lam, J. W. Y. & Tang, B. Z. Aggregation-Induced Emission:

629 New Vistas at the Aggregate Level. *Angew. Chem. Int. Ed.* **59**, 9888-9907 (2020).

630 27. Li, C. *et al.* Asymmetrical-Dendronized TADF Emitters for Efficient Non-doped

631 Solution-Processed OLEDs by Eliminating Degenerate Excited States and Creating

632 Solely Thermal Equilibrium Routes. *Angew. Chem. Int. Ed.* **134**, e202115140,

633 (2021).

634 28. Liu, F. *et al.* Highly efficient nondoped blue organic light-emitting diodes with high

635 brightness and negligible efficiency roll-off based on anthracene-triazine

636 derivatives. *J. Mater. Chem. C* **7**, 14881-14888 (2019).

637 29. Hohenberg, P., & Kohn, W. J. P. R. Density functional theory (DFT). *Phys. Rev.*

638 **136**, B864 (1964).

639 30. Stratmann, R. E., Burant, J. C., Scuseria, G. E., & Frisch, M. J. Improving harmonic

640 vibrational frequencies calculations in density functional theory. *J. Chem. Phys.* **106**,

641 10175-10183 (1997).

642 31. Lu, T. & Chen, F. Multiwfn: a multifunctional wavefunction analyzer. *J. Comput.*

643 *Chem.* **33**, 580-592 (2012).

644 32. Liu, Z., Lu, T. & Chen, Q. An sp-hybridized all-carboatomic ring, cyclo[18]carbon:

Electronic structure, electronic spectrum, and optical nonlinearity. *Carbon* **165**, 461-467 (2020).

33. Shi, Y. *et al.* Optimal Dihedral Angle in Twisted Donor-Acceptor Organic Emitters for Maximized Thermally Activated Delayed Fluorescence. *Angew. Chem. Int. Ed.* **61**, e202213463 (2022).

34. Li, J., Zhang, M., Li, T., Guo, D., Tian, T., & Zhang, H. Realization of switching between TADF and HLCT emissions through modulation of the intramolecular charge transfer character. *J. Mater. Chem. C* **10**, 13124-13136 (2022).

35. Bryce, M. R. Heavy atom effects benefit organic light emitting diode (OLED) performance. *Sci. China: Chem.* **66**, 1-3 (2022).

36. Valiev, R. R. *et al.* Fast estimation of the internal conversion rate constant in photophysical applications. *Phys. Chem. Chem. Phys.* **23**, 6344-6348 (2021).

37. Shizu, K., Ren, Y. & Kaji, H. Promoting Reverse Intersystem Crossing in Thermally Activated Delayed Fluorescence via the Heavy-Atom Effect. *J. Phys. Chem. A* **127**, 439-449 (2023).

38. Zhao, Z. *et al.* Revisiting an ancient inorganic aggregation-induced emission system: An enlightenment to clusteroluminescence. *Aggregate*, **2**, e36 (2021).

39. Wei, H. et al. Sensitive X-ray detectors made of methylammonium lead tribromide perovskite single crystals. *Nat. Photon.* **10**, 333-339 (2016).

40. Berger, M. J. et al. XCOM: Photon Cross Sections Database (National Institute of Standards and Technology, 2013); https://www.nist.gov/pml/xcom-photoncross-sectionsdatabase

41. Zhang, Y. *et al.* Efficient and Fast X-Ray Luminescence in Organic Phosphors Through High-Level Triplet-Singlet Reverse Intersystem Crossing. *CCS Chem.* **6**, 334-341 (2024).

42. Zhan, L. *et al.* Organic molecules with dual triplet-harvesting channels enable efficient X-ray scintillation and imaging. *Aggregate*, **5**, e485 (2024).

672   43. Cui, H. *et al.* Lead-free organic–inorganic hybrid scintillators for X-ray detection.

673   *Aggregate,* **5**, e454 (2023).

674   44. Zhao, W., Xiao, G. & Zou, B. Pressure-induced emission (PIE) in halide perovskites

675   toward promising applications in scintillators and solid-state lighting. *Aggregate*, 5,

676   e461 (2023).

677   45. Yuan, P. et al. Thermally activated delayed fluorescence Au-Ag-oxo nanoclusters:

678   From photoluminescence to radioluminescence. *Aggregate*, 5, e475 (2024).